Monthly Notices
of the
ROYAL ASTRONOMICAL SOCIETY

Mon. Not. R. Astron. Soc. **426,** 2129–2136 (2012) doi:10.1111/j.1365-2966.2012.21890.x

Infrared emission-line tomography of the intergalactic medium during the epoch of reionization

Koki Kakiichi, Avery Meiksin★ and Eric Tittley

SUPA†, Institute for Astronomy, University of Edinburgh, Blackford Hill, Edinburgh EH9 3HJ

Accepted 2012 August 7. Received 2012 July 27; in original form 2012 January 26

ABSTRACT

The first major star-forming galaxies and active galactic nuclei will produce Balmer and higher order extended haloes during the epoch of reionization through the scattering of Lyman resonance line photons off the surrounding neutral intergalactic gas. The optical depth dependence of the scattering rates will produce a signal sensitive to both the density and velocity fluctuations of the gas, offering the possibility of probing the ionization region and flow field surrounding young star-forming galaxies. The requirements for detecting the haloes in the infrared using a space-based telescope are discussed. A suggested experiment designed to match the Balmer halo characteristics for a field of view with a 1 arcmin radius would have a signal-to-noise ratio of $(1\text{–}3)\dot{M}_{100}t_6^{1/2}$, where $\dot{M}_{100}$ is the star formation rate in units of $100\,\mathrm{M}_\odot\,\mathrm{yr}^{-1}$ and t_6 is the exposure time in units of 10^6 s. Simultaneous measurements of multiple Balmer order haloes would reduce the integration time required for detection by a comparable factor.

Key words: atomic processes – line: formation – radiative transfer – scattering – cosmology: theory – infrared: general.

1 INTRODUCTION

The breaking of the redshift $z = 7$ barrier in the campaign to discover high-redshift galaxies is closing in on the epoch of reionization (EoR), when sufficient stars, with a possible contribution from active galactic nuclei (AGN), formed to reionize the hydrogen produced in the big bang following the recombination era. In addition to the handful of sources with spectroscopically confirmed redshifts $z > 7$ (Vanzella et al. 2011; Ono et al. 2012; Schenker et al. 2012), several plausible candidates have been identified with higher photometric redshifts extending up to $z \lesssim 9$ (McLure et al. 2011), and possibly as high as $z \simeq 10$ (Bouwens et al. 2011). Measurements of the cosmic microwave background (CMB) by the *Wilkinson Microwave Anisotropy Probe* (*WMAP*) confine the EoR, if a sudden event, to $z_r = 10.4 \pm 1.2\,(1\sigma)$ (Larson et al. 2011). Thus, the highest redshift galaxies discovered may have already entered the EoR.

In addition to ionizing the intergalactic medium (IGM), high-redshift galaxies will illuminate still neutral intergalactic hydrogen before the EoR has ended. The Lyα radiation escaping high-redshift sources will scatter in the vicinity of the sources, producing Lyα haloes with a characteristic core radius of 70 kpc at $z = 10$ (Loeb & Rybicki 1999). These haloes would be observable in the near-infrared (near-IR), with characteristic diameters of 30 arcsec. The sources will be overwhelmed by zodiacal light, but a dedicated space-based facility with narrow-band imaging could plausibly detect a halo surrounding a very bright source.

Higher energy photons emitted by the continuum of the sources will scatter as well as they redshift into local Lyman resonance frequencies. Radiative cascades following the scattering of high-order Lyman series photons will produce radiation from higher order hydrogen sequences like the Balmer and Paschen series (Meiksin 2010). The haloes will be highly extended because of the distances over which higher energy photons may travel before scattering. The Hα signal from within the inner 1 arcmin of the halo could, as for the Lyα signal, be detected by an IR detector in space. The Balmer haloes, however, have the advantages over the Lyα haloes of being both more extended and comprised of multiple orders. Combining the images for the different resolvable orders could substantially reduce the required integration times for a given source.

Since the identical structures would give rise to a 21-cm signature around a source (Madau, Meiksin & Rees 1997; Pritchard & Loeb 2011), correlating the images with radio detections using an instrument like the LOw Frequency ARray (LOFAR)[1] or the Square Kilometre Array (SKA)[2] would further enhance the detections and probe the large-scale structure of the underlying IGM as well as the ionization geometry produced by the source (Tozzi et al. 2000).

★E-mail: aam@roe.ac.uk
†Scottish Universities Physics Alliance.

[1] www.lofar.org
[2] www.skatelescope.org

The purpose of this paper is to compute the expected Balmer signals allowing for the structure of the IGM. Since the scattering rate depends on the optical depth from the source to Lyman resonance line photons, the signal will depend on the density, temperature and peculiar velocity structure of the IGM. The influence of inhomogeneities in these quantities is computed using a cosmological numerical simulation.

This paper is structured as follows. The next section summarizes the mechanism of the effect and the simulation model. A presentation of the resulting images follows. A subsequent section compares the background and local source Lyman photon collision rates that generate the haloes. The observational requirements for detecting the signal are then discussed, followed by our conclusions. In Appendix A, we derive the distribution of the fluctuations in the background Ly*n* mean intensity produced by multiple sources.

2 THE PRODUCTION OF BALMER HALOES

2.1 The Ly*n* scattering rate

The local Ly*n* radiation field within a gas parcel arises from two contributions: the direct ultraviolet (UV) photons emitted from the central radiating source redshifted to the local Ly*n* resonance frequency by the cosmological expansion and any radial peculiar velocity v_r of the gas, and the photons produced in radiative cascades following the scattering of higher order Lyman series photons. The effect of redshifting limits the distance freely streaming photons from a source may travel before scattering. From the perspective of a gas parcel at redshift z, only sources within the Lyman horizon,

$$1+z_n^{\rm hor}=(1+z)\left(1-\frac{v_r}{c}\right)\frac{1-(n+1)^{-2}}{1-n^{-2}}, \tag{1}$$

are able to excite a hydrogen atom into an electronic state with principal quantum number n (Barkana & Loeb 2005). Higher energy photons will have passed through a higher order Lyman resonance. As a result, the maximum possible distance of sources able to produce a direct scatter of Ly*n* photons decreases with increasing n as

$$D_n^{\rm hor}\simeq\frac{c}{H(z)}\frac{2n+1}{(n-1)(n+1)^3}, \tag{2}$$

for $|v_r|\ll H(z)D_n^{\rm hor}$.

Higher order Lyman photons will scatter within the Doppler core.[3] The mean free path of Ly*n* photon within the Doppler core is

$$\lambda_n^{\rm mfp}(z)=\frac{\pi^{1/2}\Delta\nu_{{\rm D},n}}{n_{\rm H}(z)\sigma_n}\simeq 0.101(1+z)^{-3}T^{1/2}n(n^2-1)\,{\rm pc}, \tag{3}$$

where $n_{\rm H}(z)$ is the hydrogen number density, $\Delta\nu_{{\rm D},n}=\nu_n b/c$ is the Doppler width with Doppler parameter $b=(2kT/m_{\rm H})^{1/2}$ for gas temperature T and $\sigma_n=(\pi e^2/m_{\rm e}c)f_{1n}$ for oscillator strength f_{1n} (Meiksin 2009). The approximation $f_{1n}\simeq 1.56n^{-3}$ was used, accurate to better than 10 per cent for $n>4$. The mean free path is much smaller than the Jeans length $\lambda_{\rm J}=c_{\rm s}(\pi/G\rho_{\rm M})^{1/2}\simeq 16(1+z)^{-3/2}T^{1/2}$ kpc for a sound speed $c_{\rm s}$ and cosmic mass density $\rho_{\rm M}$ over which the physical properties of the IGM will be nearly uniform. The redistribution of photon energy from scatters may thus be considered to occur locally, confined within a homogeneous medium. A higher order photon will scatter only a few times before decaying into a lower order photon, with a survival probability of ∼0.8 per scatter (Hirata 2006; Pritchard & Furlanetto 2006), so that the effects of spatial and frequency diffusion, redshifting and evolution of the IGM will be negligible before the photon is destroyed.

Including photons produced in cascades from higher orders, the net scattering rate of Ly*n* photons is

$$P_n=\frac{1}{1-p_{nn}}\left[P_n^{(1)}+\sum_{n'>n}^{n_{\rm max}}p_{n'n}P_{n'}\right] \tag{4}$$

for a maximum order $n_{\rm max}$ of directly scattered Lyman resonance line photons, where $P_n^{(1)}$ is the direct scattering rate:

$$P_n^{(1)}=P_n^{\rm inc}(0)\mathcal{S}_n, \tag{5}$$

with $P_n^{\rm inc}(0)=\sigma_n L_{\nu_n}/(4\pi r_{\rm L}^2 h\nu_n)$ the scattering rate at the luminosity distance $r_{\rm L}$ from a source of specific luminosity $L_{\nu_n(1+z_{\rm s})/(1+z)}$ assuming no intergalactic attenuation (Meiksin 2010). Here, $\mathcal{S}_n$ accounts for the intergalactic attenuation and $p_{n'n}$ is the probability that a Lyn' photon converts into a Ly*n* photon per scatter.

The scattering rate may be expressed more succinctly in terms of the direct scattering rates as

$$P_n=\frac{1}{1-p_{nn}}\sum_{n'=n}^{n_{\rm max}}\mathcal{C}_{n'n}P_{n'}^{(1)}, \tag{6}$$

where the scattering cascade matrix $\mathcal{C}_{n'n}$ has been defined according to

$$\mathcal{C}_{n'n}=\sum_{n''>n}^{n'}\mathcal{C}_{n'n''}\eta_{n''n}, \tag{7}$$

with $\mathcal{C}_{nn}=1$, $\mathcal{C}_{n'n}=0$ for $n>n'$ and $\eta_{n'n}=p_{n'n}/(1-p_{n'n'})$.

The suppression factor $\mathcal{S}_n$ is given by

$$\mathcal{S}_n=\int_0^\infty {\rm d}\nu\,\varphi_{\nu_n}(a_n,\nu-\nu_n){\rm e}^{-\tau_n(\nu,z;z_{\rm s})}, \tag{8}$$

where $\varphi_{\nu_n}(a_n,\nu-\nu_n)=(\Delta\nu_{{\rm D},n})^{-1}\phi(a_n,x)$ is the Voigt profile with $x=(\nu-\nu_n)/\Delta\nu_{{\rm D},n}$ and a_n is the ratio between the damping width and Doppler width for Ly*n* photons. Within the Doppler core, $\phi(a_n,x)\simeq\pi^{-1/2}\exp(-x^2)$, while in the Lorentz wings $\phi(a_n,x)\simeq a_n/\pi x^2$. The optical depth is given by

$$\tau_n(\nu,z;z_{\rm s})=\sigma_n\int_z^{z_{\rm s}}{\rm d}z'\frac{{\rm d}l}{{\rm d}z'}n_{\rm H}(z')\times\varphi_{\nu n}\left[a_n(T'),\nu\frac{1-v_r'/c}{1-v_r/c}\frac{1+z'}{1+z}\right]. \tag{9}$$

In the wing approximation, the optical depth rapidly approaches $\tau_n\simeq x_{1n}/x$ with distance from the source, where $x_{1n}=(a_n/\pi)(\sigma_n c/\nu_n)[n_{\rm H}(z)/H(z)]$ (Higgins & Meiksin 2009). Then $\mathcal{S}_n\simeq\gamma_n$, where $\gamma_n=H(z)/[\lambda_n\sigma_n n_{\rm H}(z)]$ is the Ly*n* Sobolev parameter. Because Ly*n* photons are first scattered predominantly in the Doppler core for $n>4$, γ_n overestimates $\mathcal{S}_n$ by about a factor of 2 for $n>4$ (cf. table 2 in Meiksin 2010).

2.2 The halo emissivities

The emissivities depend on the populations $n_{n,l}$ of the excited states, where the subscripts indicate the principal quantum number and orbital angular momentum, respectively, of a given fine-structure

[3] At $z=8$, for an IGM temperature $T>10$ K (100 K), Lyδ (Lyγ) and higher order Lyman resonance line photons scatter in the Doppler core (Meiksin 2010).

state of an excited hydrogen atom. The equations governing the populations are, for the ground state n_1,

$$\frac{\mathrm{d}n_1}{\mathrm{d}t} = \sum_{n=2}^{n_{\max}} n_{n,1} A_{n1,10} - n_1 \sum_{n=2}^{n_{\max}} P_n, \tag{10}$$

and for excited states,

$$\frac{\mathrm{d}n_{n,l}}{\mathrm{d}t} = n_1 P_n \delta_{l,1} + \sum_{n'=n+1}^{n_{\max}} \sum_{l'=l\pm1} n_{n',l'} A_{n'l',nl} - n_{n,l} \sum_{n'=1}^{n-1} \sum_{l'=l\pm1} A_{nl,n'l'}, \tag{11}$$

where $\delta_{l,l'} = 1$ for $l = l'$ and vanishes otherwise. Here, $A_{nl,n'l'}$ is the spontaneous decay rate from level n, l to level n', l'.

The level populations will establish their steady-state values on the time-scales P_n^{-1}. The system of steady-state equations is solved by

$$n_{n,l} = \sum_{n'=n}^{n_{\mathrm{mex}}} n_1 P_{n'} \frac{C_{n'1,nl}}{\sum_{n'=1}^{n-1} \sum_{l'=l\pm1} A_{nl,n'l'}}, \tag{12}$$

where $C_{n'l',nl}$ is the cascade matrix expressing the probability that an upper state n', l' cascades down to a lower state n, l via all possible transition routes. It is given by

$$C_{n'1,nl} = \sum_{n''=n+1}^{n'} \sum_{l''=l\pm1} C_{n'1,n''l''} \alpha_{n''l'',nl}, \tag{13}$$

with $C_{nl',nl} = \delta_{l,l'}$, where $\alpha_{n'l',nl} = A_{n'l',nl} / \sum_{n''=1}^{n'-1} \sum_{l''=l'\pm1} A_{n'l',n''l''}$ is the branching ratio from level $n'l'$ to level nl (cf. Osterbrock 1989). The transition rates $A_{n'l',nl}$ are computed as in Meiksin (2010).

The resulting emissivity due to all transitions from n to n' with mean frequency $\nu_{nn'}$ is

$$\epsilon_{nn'} = \frac{h\nu_{nn'}}{4\pi} \sum_{l} \sum_{l'=l\pm1} n_{n,l} A_{nl,n'l'} = \frac{h\nu_{nn'}}{4\pi} n_1 \sum_{l} \sum_{l'=l\pm1} \beta_{nl} \alpha_{nl,n'l'}, \tag{14}$$

where $\beta_{nl} = \sum_{n'=n}^{n_{\max}} P_{n'} C_{n'1,nl}$. The observed specific intensity is then

$$j_\nu \simeq \int_0^\infty \mathrm{d}z \frac{\mathrm{d}l_{\mathrm{p}}}{\mathrm{d}z} (1+z)^{-3} \epsilon_{nn'}(l_{\mathrm{p}}) \times \varphi_{\nu_{nn'}} \left[\nu \left(1 + \frac{v_\parallel}{c} \right) (1+z) - \nu_{nn'} \right], \tag{15}$$

for emission along the line-of-sight path l_{p} with line-of-sight velocity $v_\parallel$.

3 INFRARED EMISSION TOMOGRAPHY

The optical depth is sensitive to the density, temperature and peculiar velocity fields. As a consequence, fluctuations in these quantities between the source and a given gas parcel will produce fluctuations in the scattering rate through equations (5) and (6). These in turn will produce fluctuations in the emissivity of the resulting cascade radiation, opening up the opportunity to measure the density, temperature and peculiar velocity fields on small scales surrounding a source.

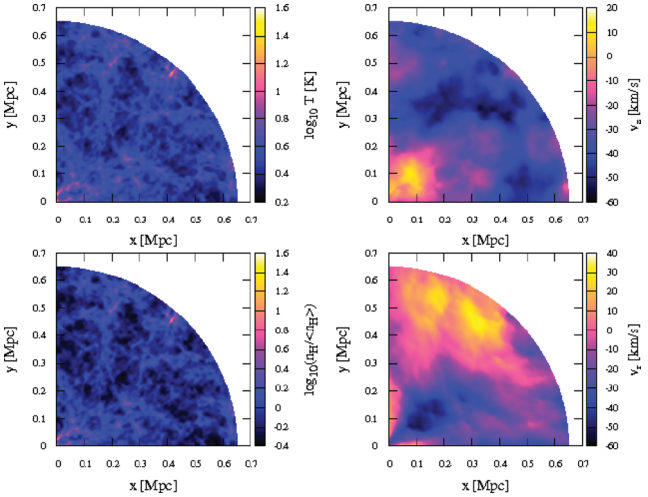

Figure 1. Clockwise from the top left: the temperature, tangential (single-component) peculiar velocity, radial peculiar velocity and density fields of IGM around a radiating source at $z = 10$ placed at the origin. (Distance units are proper.)

3.1 Numerical simulation

In order to estimate the magnitude of the effect of the fluctuations on the received intensity, we use a numerical cosmological Λ cold dark matter (ΛCDM) simulation of the IGM to compute the signal predicted from the surroundings of a source placed in the simulation volume. The simulation was run using version 1.0.1 of ENZO[4] with the cosmological parameter values $\Omega_{\mathrm{m}} = 0.236$, $\Omega_{\mathrm{v}} = 0.764$ and $\Omega_{\mathrm{b}} = 0.041$ for the matter, vacuum energy and baryonic matter density parameters, a Hubble constant $H_0 = 100\,h\,\mathrm{km\,s^{-1}\,Mpc^{-1}}$, with $h = 0.73$, and the initial BBKS power spectrum with $n = 0.95$ normalized to $\sigma_8 = 0.74$, generally consistent with CMB fluctuations as measured by *WMAP* (Larson et al. 2011). The simulation was run in a volume $10\,h^{-1}\,\mathrm{Mpc}$ on a side with 256^3 cells and 512^3 dark matter particles. The volume was evolved from an initial redshift of $z_{\mathrm{i}} = 530$ to $z = 10$. The initial mean temperature is set to $550\,\mathrm{K}\,[(1+z_{\mathrm{i}})/(1+200)]^2 \simeq 3800\,\mathrm{K}$, and evolves to $T \simeq 2\,\mathrm{K}$ by $z = 10$. Radiative cooling permits collapse of gas in haloes, but there is no feedback from star formation.

A source was assigned to the highest gas density peak within the simulation volume at $z = 10$, as recorded on the gas grid with cells of size $10/256\,\mathrm{Mpc}\,h^{-1} \simeq 40\,\mathrm{kpc}\,h^{-1}$ per side comoving. The corresponding density, temperature and peculiar velocity fields in a quadrant around the source are shown for a slice in Fig. 1, with representative line-of-sight values shown in Fig. 2.

The source is modelled as a starburst galaxy with a specific intensity approximated as flat at the relevant frequencies, so that the source intensity at a luminosity distance r_{L} is

$$\mathcal{S}_\nu = \frac{L_{\nu_{\mathrm{L}}}}{(4\pi)^2 r_{\mathrm{L}}^2}, \tag{16}$$

where $L_{\nu_{\mathrm{L}}}$ is the luminosity at the Lyman edge frequency ν_{L}. A continuous star formation rate $10\,\mathrm{M_\odot\,yr^{-1}}$ is assumed, with a Salpeter initial mass function (IMF) for the range $1 < M < 100\,\mathrm{M_\odot}$ and a metallicity $Z = 0.05\,\mathrm{Z_\odot}$, corresponding to $L_{\nu_{\mathrm{L}}} = 3.8 \times 10^{21}\,\mathrm{W\,Hz^{-1}}$ after $10^7\,\mathrm{yr}$ (Leitherer et al. 1999). For future reference, the production rate of hydrogen-ionizing photons is

[4] Available from http://lca.ucsd.edu.

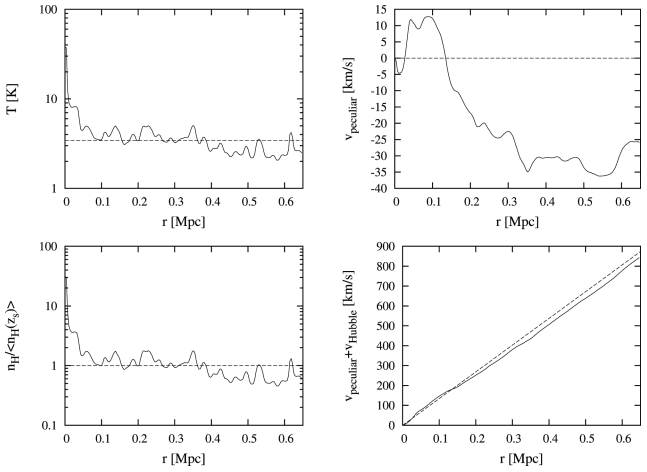

Figure 2. Clockwise from the top left: representative line-of-sight variations in the temperature, peculiar velocity, total velocity (including Hubble flow) and density of IGM around a radiating source at the origin, drawn from the simulation in Fig. 1. The dotted lines are the corresponding values for a homogeneous expanding medium. (Distance units are proper.)

$\dot{N}_\gamma \simeq 3.4 \times 10^{54}\,\mathrm{s}^{-1}$, corresponding to an effective ionizing spectral index $\alpha_{\rm eff} = L_{\nu_{\rm L}}/h\dot{N}_\gamma \simeq 1.7$.

The $10\,h^{-1}$ Mpc simulation box size is too small to properly capture the peculiar velocities of the dark matter and the gas. The peculiar velocity fields of the collapsing regions relative to the central high-redshift galaxies, however, are expected not to be much affected by the missing power. We thus expect the qualitative features of the Balmer haloes to be well reproduced by the simulation.

3.2 Emission-line haloes

The resulting scattering rates of Ly*n* photons differ substantially from those for a homogeneous expanding medium, as shown in Fig. 3. The contributions due to the density, temperature and velocity departures from the mean are broken down in the figure. While the differences are primarily due to the density fluctuations, fluctuations in the temperature and expansion velocity contribute non-negligibly. In particular, the scattering rate becomes increasingly sensitive to the peculiar velocity field towards the higher orders, for which scattering in the Doppler core dominates increasingly over Lorentz

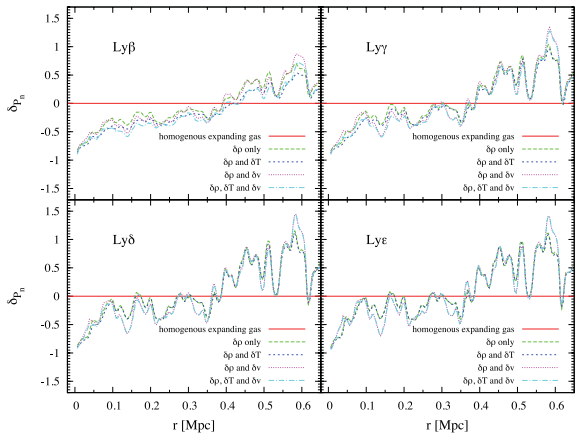

Figure 3. The relative difference between the Ly*n* scattering rate along the ray in Fig. 2 and the corresponding rate assuming a homogeneous expanding medium.

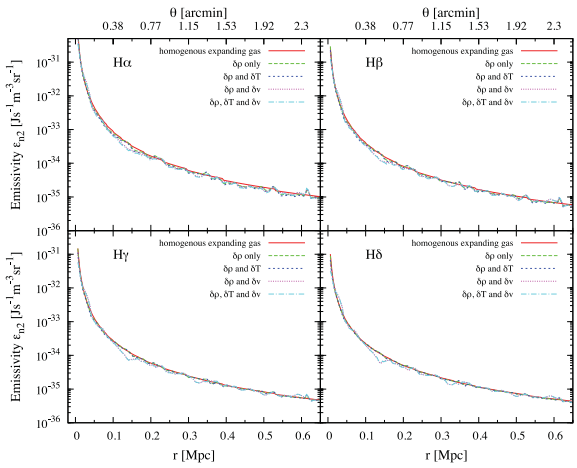

Figure 4. Comparison between the H*n* emissivity along the ray in Fig. 2 and the corresponding rate assuming a homogeneous expanding medium.

wing scattering. As the optical depth increases with decreasing total velocity gradient, regions with a peculiar velocity gradient $\mathrm{d}v/\mathrm{d}r < 0$ tend to have a suppressed scattering rate compared with regions with $\mathrm{d}v/\mathrm{d}r > 0$. This may be seen by comparing the fluctuations in the scattering rate in Fig. 3 with the slope in the total velocity shown in the lower-right panel of Fig. 2.

The Balmer emissivity profiles for Hα through Hδ are shown in Fig. 4 for the ray shown in Fig. 2. The fluctuations follow those in the Ly*n* scattering rates, but are somewhat suppressed in magnitude, as shown in Fig. 5. This is because, while the emissivity is proportional to the local gas density, so that fluctuations in the emissivity include a linear dependence on the density fluctuations, the scattering rate fluctuates oppositely to the density fluctuations because of the effect of the optical depth variations. The sum of the contributions to the relative fluctuations in the emissivity is thus reduced compared with the magnitude of the relative density fluctuations.

The derivation of the surface brightness is computationally intensive, as the cascade equations must be solved separately within each simulation cell. For this reason the computation is restricted to a plane perpendicular to the line of sight. A narrow-band filter would include contributions from the nearby foreground and background regions as well. Modelling a specific filter arrangement would require further layers to be included for a realistic estimate,

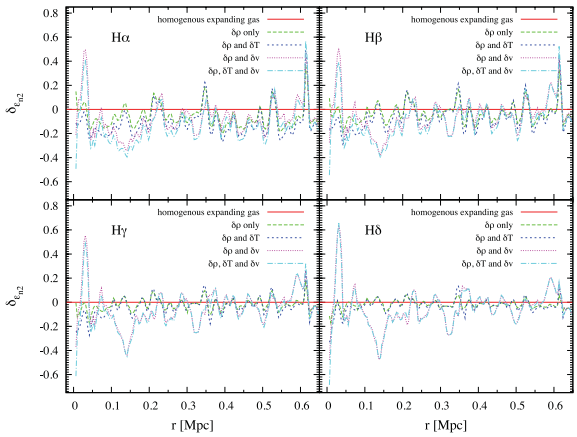

Figure 5. Relative difference between the H*n* emissivity along the ray in Fig. 2 and the corresponding emission assuming a homogeneous expanding medium.

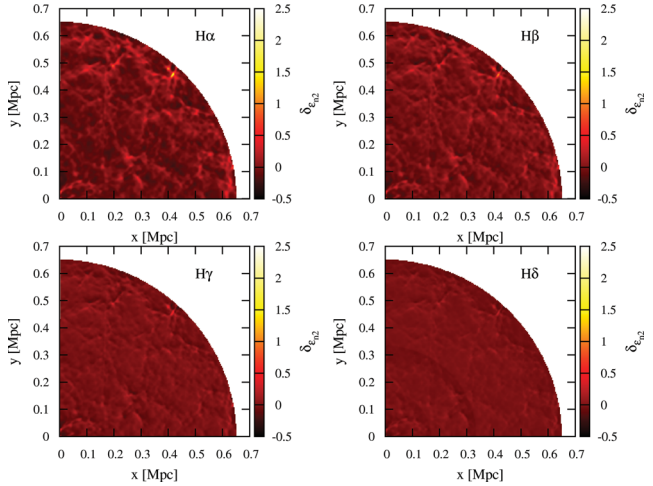

Figure 6. Differential Balmer surface brightness fluctuations compared with the homogeneous expanding IGM case allowing only for the density fluctuation contribution.

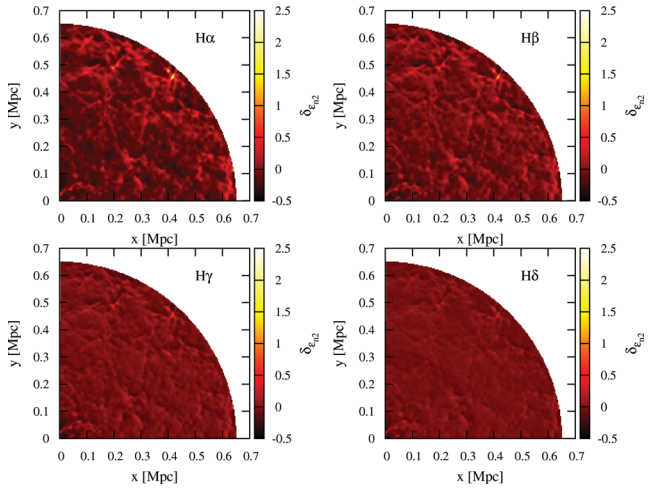

Figure 7. Differential Balmer surface brightness fluctuations compared with the homogeneous expanding IGM case allowing only for the density and temperature fluctuation contributions.

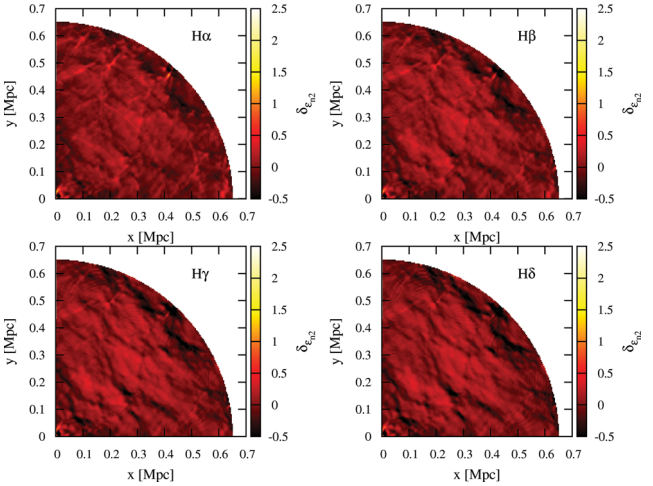

Figure 8. Differential Balmer surface brightness fluctuations compared with the homogeneous expanding IGM case allowing only for the density and velocity fluctuation contributions.

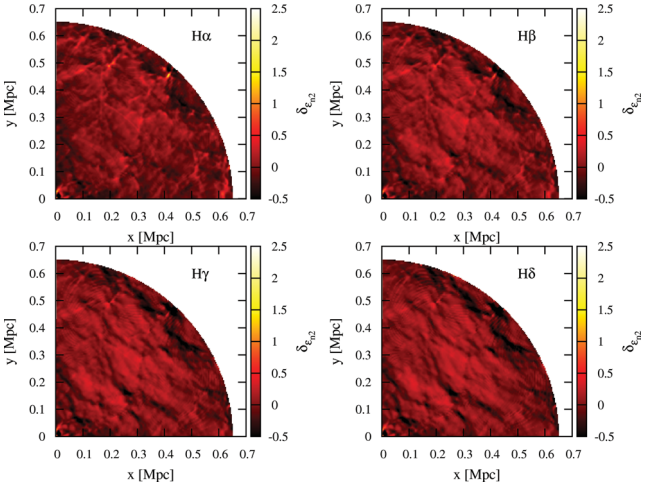

Figure 9. Differential Balmer surface brightness fluctuations compared with the homogeneous expanding IGM case allowing for the effects of density, temperature and velocity fluctuations.

which would tend to blur the image if the filter width corresponded to a length scale that exceeds the coherence scale of the inhomogeneities. The results shown here are thus only representative of the magnitude of the effects that should arise from inhomogeneities in the density, temperature and peculiar velocity fields.

The effects of the density, temperature and velocity fluctuations on the Balmer surface brightnesses are illustrated in the differential maps shown in Figs 6–9. The maps show the differences from the case for a homogeneous expanding IGM. The differential map allowing only for the density fluctuations shows the suppression by the increased optical depth in dense regions, as in Fig. 5. Adding in the contribution of the temperature fluctuations substantially enhances the structures. Adding the peculiar velocity contribution to the density emphasizes differentials in the structures, allowing the possibility of tracing the peculiar velocity field around forming galaxies on small scales.

The combined map is shown in Fig. 10. The rippling effect of the IGM is clearly discernable. The influence of the peculiar velocity becomes increasingly strong for the higher orders, where the dominant scattering producing the signals moves from the Voigt wings to the Doppler core.

4 CONTRIBUTION OF LYMAN BACKGROUND RADIATION

The Ly*n* photons from sources within the Ly*n* horizon will contribute to the total Ly*n* scattering rate around a given source, which will then increase the total brightness of Balmer haloes. To estimate the magnitude of this effect, we calibrate the average background luminosity assuming a given H II porosity parameter $Q_{\rm H\,II}$, which matches the H II filling factor when less than unity. For a constant comoving source emissivity, $Q_{\rm H\,II} \simeq n_{\rm s}(> M_{\rm min}|z)\dot{N}_{\rm ion}t_{\rm H}/[\bar{n}_{\rm H}(0)(1+\tau_{\rm H})]$, where $n_{\rm s}\dot{N}_{\rm ion}$ is the ionizing photon emissivity of the sources with proper halo number density $n_{\rm s}(> M_{\rm min}) = \int_{M_{\rm min}}^{\infty}(\mathrm{d}n/\mathrm{d}M)\,\mathrm{d}M$ for halo masses greater than $M_{\rm min}$ and $\tau_{\rm H}$ is the Hubble time $t_{\rm H}(z) = 2/3H(z)$ measured in units of the average recombination time-scale $\bar{t}_{\rm rec} = [\alpha_B n_{\rm H}(z)C(z)]^{-1}$ for a clumping factor $C(z)$ (Meiksin 2009). Over $6 < z < 14$, $\tau_{\rm H} \simeq 4$–5.

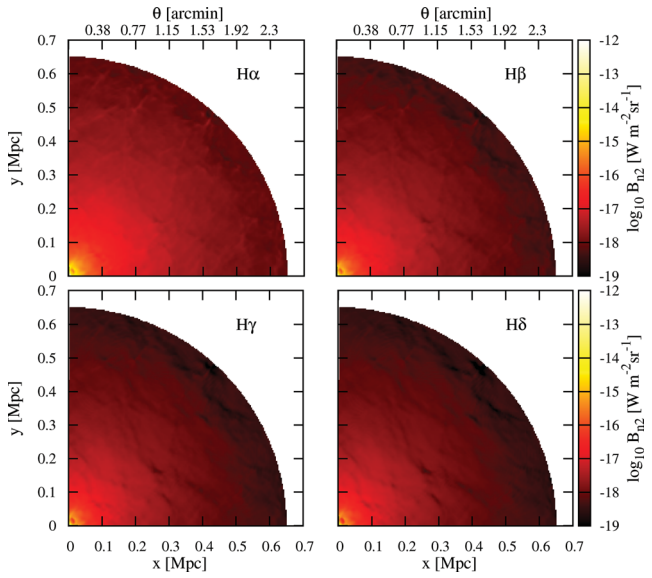

Figure 10. Balmer surface brightnesses including the effects of density, temperature and velocity fluctuations.

At $z = 10$, the mean comoving separation of haloes with mass above $10^8\,\mathrm{M}_\odot$ is ∼1 Mpc (Reed et al. 2007). This is comparable to the halo–halo correlation length (Reed et al. 2009). For halo masses exceeding $10^9\,\mathrm{M}_\odot$, the mean separation will exceed the correlation length. The sources may then be treated as unclustered to good approximation. As shown in Appendix A, the Ly*n* background mean intensity due to sources Poisson distributed in space is given by

$$\langle J_n\rangle = n_\mathrm{s}\frac{\bar{L}_n}{4\pi}\int_0^{D_n^\mathrm{hor}} \mathrm{e}^{-\tau_n(r)}\,\mathrm{d}r, \tag{17}$$

where D_n^hor is the proper Ly*n* horizon. The corresponding mean direct scattering rate due to the background is then

$$\begin{aligned} P_n^{(1),\mathrm{BG}} &= \sigma_n\int \mathrm{d}x\,\phi(a_n,x)\frac{4\pi\langle J_n\rangle}{h\nu_n}\\ &\simeq \frac{3}{2}\frac{D_n^\mathrm{hor}}{c/H(z)}H_0\Omega_\mathrm{m}^{1/2}\alpha_\mathrm{eff}(1+\tau_\mathrm{H})\frac{Q_\mathrm{H\,II}}{f_\mathrm{esc}}(1+z)^{-3/2}\\ &\simeq \frac{3}{2}H_0\Omega_\mathrm{m}^{1/2}\alpha_\mathrm{eff}(1+\tau_\mathrm{H})\frac{Q_\mathrm{H\,II}}{f_\mathrm{esc}}(1+z)^{-3/2}\frac{2n+1}{(n-1)(n+1)^3}, \end{aligned} \tag{18}$$

where we have assumed that the Lyman series portion of the spectrum is flat across the Lyman edge and the product $n_\mathrm{s}L_{\nu_\mathrm{L}}$ has been expressed in terms of the porosity $Q_\mathrm{H\,II}$, allowing for an escape fraction f_esc of ionizing photons from the galaxies.

The background scattering rate may be compared to that due to a single source as given by equation (5). For our fiducial value $L_{\nu_\mathrm{L}} = 3.8\times10^{21}\,\mathrm{W\,Hz^{-1}}$ at the Lyman edge, the ratio of Lyβ rates is

$$\frac{P_\beta^{(1)}}{P_\beta^{(1),\mathrm{BG}}} \simeq 23\left(\frac{f_\mathrm{esc}}{Q_\mathrm{H\,II}}\right)r_\mathrm{L,Mpc}^{-2}, \tag{19}$$

where $r_\mathrm{L,Mpc}$ is the distance from the source in Mpc and $\tau_\mathrm{H} \simeq 4.5$ was adopted. For $Q_\mathrm{H\,II} = 0.1$ and a typical escape fraction of $f_\mathrm{esc} = 0.1$, the source will dominate the background within a proper distance of ∼4.8 Mpc.

Table 1. Estimated photon flux (photon $\mathrm{m^{-2}\,s^{-1}}$) from low-level zodiacal light and the integrated halo flux within 1 arcmin of a starburst at $z = 8$, through an aperture of solid angle π arcmin^2 and narrow-band filter with resolution $\lambda/\Delta\lambda = 500$. The starburst is normalized to a star formation rate of $100\dot{M}_{100}\,\mathrm{M}_\odot\,\mathrm{yr^{-1}}$ over $1 < M < 100\,\mathrm{M}_\odot$ with a Salpeter IMF and metallicity $Z = 0.05\,\mathrm{Z}_\odot$. The last row provides the S/N after an integration time t_4 in units of 10^4 s for flux incident on a mirror and detector with effective collecting area 25 m^2. An IGM temperature $T = 100$ K is assumed.

Source	Hα 5.91 μm	Hβ 4.38 μm	Hγ 3.91 μm	Hδ 3.69 μm
Zodiacal	9400	1500	700	510
Halo	0.050	0.018	0.010	0.0077
S/N/$\dot{M}_{100}$	$0.26t_4^{1/2}$	$0.23t_4^{1/2}$	$0.20t_4^{1/2}$	$0.17t_4^{1/2}$

5 DETECTION OF INFRARED EMISSION HALOES

The Balmer emission lines produced in the diffuse IGM by galaxies during the EoR will redshift to the IR. In this section, an estimate is made for the requirements to detect the haloes. It is assumed that the detector is limited by photon noise, which will be dominated by IR foregrounds, primarily zodiacal light for a telescope in space. A fiducial collecting area of $A_\mathrm{fid} = 25$ m^2 is adopted with a field of view of $\mathrm{FOV_{fid}} = \pi$ arcmin^2. The field of view defines a characteristic length scale and a corresponding velocity scale given by the Hubble flow across the length scale. Imaging using a narrow-band filter of resolution $R = \lambda/\Delta\lambda = 500$ is assumed, optimized to capture the emitted flux within the field of view while minimizing the zodiacal light foreground contamination. Increasing the resolution further would decrease the signal and noise similarly, and thus reduce the signal-to-noise ratio (S/N) by $R^{-1/2}$. Reducing the resolution would capture an increasing amount of foreground light but add little to the signal, and thus reduce the S/N by $R^{1/2}$. Decreasing the field of view will generally increase the S/N for the optimal resolution by an amount depending on the transition order, as $\mathrm{FOV}^{-\alpha/2}$ with $\alpha =$ 1/3, 1/4, 1/5 and 1/6 for Hα, Hβ, Hγ and Hδ, respectively (Meiksin 2010).

Estimates for the zodiacal light foreground[5] based on the model of Wright (1998) are converted to count rates in Tables 1 and 2. The intensity of zodiacal light depends on the position and pointing direction of a satellite. The lower estimates are quoted here.

Lyman break galaxies and Lyα emitters at $z > 6$ suggest star formation rates of up to $30\,\mathrm{M}_\odot\,\mathrm{yr^{-1}}$ (González et al. 2011; McLure et al. 2011). Much higher star formation rates are known in the lower redshift Universe, reaching values of 500–1000 $\mathrm{M}_\odot\,\mathrm{yr^{-1}}$, but these are associated with ultraluminous infrared galaxies (ULIRGs) in dusty environments, which severely attenuate the UV radiation (Kennicutt 1998). On the other hand, by $z = 1$–2 ULIRGs are found to be much more transparent to UV radiation (Daddi et al. 2007). Accordingly, our estimates are normalized to a source with a star formation rate of $100\,\mathrm{M}_\odot\,\mathrm{yr^{-1}}$.

The resulting lower order Balmer fluxes are shown in Tables 1 and 2 at redshifts $z = 8$ and 10, respectively, using the methodology of Meiksin (2010). The corresponding S/N values after integrating over a time t are provided in the last row of the table. The S/N decreases

[5] At http://jwstetc.stsci.edu/etcstatic/users_guide/t8_background.html.

Table 2. Estimated photon flux (photon $m^{-2}\,s^{-1}$) from low-level zodiacal light and the integrated halo flux within 1 arcmin of a starburst at $z = 10$, through an aperture of solid angle πarcmin^2 and narrow-band filter with resolution $\lambda/\Delta\lambda = 500$. The starburst is normalized to a star formation rate of $100\dot{M}_{100}\,M_\odot\,yr^{-1}$ over $1 < M < 100\,M_\odot$ with a Salpeter IMF and metallicity $Z = 0.05\,Z_\odot$. The last row provides the S/N after an integration time t_4 in units of 10^4 s for flux incident on a mirror and detector with effective collecting area 25 m^2. An IGM temperature $T = 100$ K is assumed.

Source	Hα 7.22 μm	Hβ 5.35 μm	Hγ 4.78 μm	Hδ 4.51 μm
Zodiacal	2.5×10^4	5400	2300	1900
Halo	0.041	0.015	0.0085	0.0064
S/N/$\dot{M}_{100}$	$0.13t_4^{1/2}$	$0.099t_4^{1/2}$	$0.088t_4^{1/2}$	$0.074t_4^{1/2}$

only weakly with the Balmer order. A starburst of $300\,M_\odot\,yr^{-1}$ would require an integration time of 0.4×10^6 s for a 5σ detection at $z = 8$. At $z = 10$, the integration time increases to 1.6×10^6 s. Allowing for the stacking of multiple bands in an instrument that split the beam into a range of bands tuned to correspond to the different Balmer series would reduce the required integration time for detection approximately by the number of bands stacked.

These observations are more demanding than for Lyα haloes (Loeb & Rybicki 1999). The haloes have surface brightness cores of about $0.1r_* \simeq 110$ kpc, corresponding to angular diameters of 40–50 arcsec at $z = 8$–10, beyond which the surface brightness rapidly declines. The spectral full width at half-maximum corresponds to $\lambda/\Delta\lambda \simeq 110$–150. Allowing for a conversion factor of hydrogen ionizing photons into Lyα photons of about 0.65 (Osterbrock 1989), a starburst galaxy forming stars with a Salpeter IMF and metallicity $Z = 0.05\,Z_\odot$ continuously will produce Lyα photons at the rate $\dot{N}_\alpha \simeq 2.3 \times 10^{55}\,s^{-1}$, normalized to a star formation rate of 100 $M_\odot\,yr^{-1}$ with masses $1 < M < 100\,M_\odot$ (Leitherer et al. 1999). For a telescope aperture matching the core diameters, we estimate a Lyα photon flux at 1.1 μm of 0.14 photon $m^{-2}\,s^{-1}$ for a source at $z = 8$, and 0.096 photon $m^{-2}\,s^{-1}$ at 1.3 μm for a source at $z = 10$. Allowing for a spectral resolution of $R = 50$ to capture the bolometric luminosity of the source, the corresponding zodiacal light fluxes are 1600–1700 photon $m^{-2}\,s^{-1}$. For a 25 m^2 aperture telescope, the S/N values will be 1.6 and $1.2t_4^{1/2}$ at $z = 8$ and 10, respectively. These are factors of 5–10 higher than for the Balmer haloes, although over more localized regions surrounding the source which may have been ionized by the source. The estimates also assume that all the Lyα photons escape, while dust internal to the sources may absorb a large fraction of the photons.

6 CONCLUSIONS

The search for the highest redshift galaxies may have identified forming galaxies responsible at least for a large component of the reionization of the IGM. Establishing that the IGM was actually neutral, however, requires direct detection of the neutral medium. A major goal of existing and planned radio facilities is to detect the neutral IGM 21-cm signal from the EoR. A complementary path is to discover the UV light from the sources reradiated by the IGM and received as IR radiation. Rescattered Lyα photons offer one possibility, although the emission is restricted by the spatial diffusion of the photons to the vicinity of the source. Higher energy photons will redshift into local higher order Lyman series photons, exciting extended Balmer and higher order emission-line haloes through electron cascades following Lyman photon scattering.

We have shown that the fluctuations in the signal are sensitive not only to the density fluctuations in the surrounding gas through the mean free path of the scattered Lyman photons, but to the velocity field as well. This offers the possibility of mapping out both the ionization structure and the peculiar velocity field, produced by inflows or wind-driven outflows, surrounding the earliest major radiation sources, whether galaxies or AGN.

The principal obstacle to the detection of the IR haloes is the zodiacal light foreground. The ideal observing instrument would be a space telescope with an effective collecting area of at least 25 m^2, a field of view of a few to several square arcminutes and a detector sensitive to the wavelength range 3–8 μm with the capability of simultaneous imaging in several narrow tunable bands with a resolution of $R \simeq 500$. Basing an estimate on a pointing to a region of sky with a low level of zodiacal light foreground, we find that a $300\,M_\odot\,yr^{-1}$ starburst galaxy could be detected at the 5σ level in a single band in a 0.4×10^6 s integration at $z = 8$ or a 1.6×10^6 s integration at $z = 10$. Observing the object simultaneously in four bands would reduce the integration times by a comparable factor.

The haloes could plausibly be detected by an instrument similar to the originally designed Tunable Filter Imager[6] for the *James Webb Space Telescope* (*JWST*), although with a somewhat broader wavelength coverage and narrower filter. A special-purpose built telescope with a comparable mirror and optical throughput employing such a filter would be able to detect neutral haloes around the brighter sources, and thus establish the EoR.

ACKNOWLEDGMENTS

KK acknowledges support from the Mie Prefecture of Japan for a Study-abroad Scholarship, and thanks the Robert Cormack Bequest for an Undergraduate Summer Vacation Research Scholarship. ET is supported by an STFC Rolling Grant.

REFERENCES

Barkana R., Loeb A., 2005, ApJ, 626, 1
Bouwens R. J. et al., 2011, Nat, 469, 504
Daddi E. et al., 2007, ApJ, 670, 156
González V., Labbé I., Bouwens R. J., Illingworth G., Franx M., Kriek M., 2011, ApJ, 735, L34
Higgins J., Meiksin A., 2009, MNRAS, 393, 949
Hirata C. M., 2006, MNRAS, 367, 259
Kennicutt R. C., Jr, 1998, ARA&A, 36, 189
Larson D. et al., 2011, ApJS, 192, 16
Leitherer C. et al., 1999, ApJS, 123, 3
Loeb A., Rybicki G. B., 1999, ApJ, 524, 527
McLure R. J. et al., 2011, MNRAS, 418, 2074
Madau P., Meiksin A., Rees M. J., 1997, ApJ, 475, 429
Meiksin A. A., 2009, Rev. Mod. Phys., 81, 1405
Meiksin A., 2010, MNRAS, 402, 1780
Meiksin A., White M., 2003, MNRAS, 342, 1205
Ono Y. et al., 2012, ApJ, 744, 83
Osterbrock D. E., 1989, Astrophysics of Gaseous Nebulae and Active Galactic Nuclei. University Science Books, Mill Valley, CA
Pritchard J. R., Furlanetto S. R., 2006, MNRAS, 367, 1057
Pritchard J. R., Loeb A., 2012, Rep. Prog. Phys., 75, 086901

[6] The filter that is to be installed now on *JWST* is much more restricted. The original design is at http://www.stsci.edu/jwst/doc-archive/handbooks/JWST_Primer_v20.pdf.

Reed D. S., Bower R., Frenk C. S., Jenkins A., Theuns T., 2007, MNRAS, 374, 2
Reed D. S., Bower R., Frenk C. S., Jenkins A., Theuns T., 2009, MNRAS, 394, 624
Schenker M. A., Stark D. P., Ellis R. S., Robertson B. E., Dunlop J. S., McLure R. J., Kneib J.-P., Richard J., 2012, ApJ, 744, 179
Tozzi P., Madau P., Meiksin A., Rees M. J., 2000, ApJ, 528, 597
Vanzella E. et al., 2011, ApJ, 730, L35
Wright E. L., 1998, ApJ, 496, 1
Zuo L., 1992, MNRAS, 258, 36

APPENDIX A: STATISTICAL METHOD: LYMAN BACKGROUND RADIATION FIELD

We follow the statistical method of Zuo (1992) and Meiksin & White (2003) to estimate the Ly*n* background radiation field. Consider a spherical patch in the universe with proper radius R with a central source at the origin containing N sources. The number of sources fluctuates over various patches according to the Poisson distribution $P(N) = (\bar{N}^N \mathrm{e}^{-\bar{N}})/N!$ with mean value $\bar{N}$. The total radiation field at the origin is $J = \sum_{k=1}^{N} j_k$, $j_k = L_k \mathrm{e}^{-\tau(r_k)}/(4\pi r_k)^2$. The probability distribution function of the total specific intensity J given N sources is $P(J|N)$. The characteristic function $\mathcal{C}(t|N) = \int_0^\infty \mathrm{e}^{\mathrm{i}tJ} P(J|N)\mathrm{d}J$. If the specific intensities of the sources are statistically independent of each other, we may express $P(J|N)$ as

$$P(J|N)\ \mathrm{d}J = \prod_{k=1}^{N} p(j_k)\ \mathrm{d}j_k. \tag{A1}$$

Then, the characteristic function simplifies to

$$\mathcal{C}(t|N) = \prod_{k=1}^{N} \int_0^\infty \mathrm{e}^{\mathrm{i}tj_k} p(j_k)\ \mathrm{d}j_k, \tag{A2}$$

or $\mathcal{C}(t|N) = \mathcal{C}_1(t)^N$, where the one-source characteristic function is defined as

$$\mathcal{C}_1(t) = \int_0^\infty \mathrm{e}^{\mathrm{i}tj} p(j)\ \mathrm{d}j, \tag{A3}$$

suppressing the index k.

Marginalizing over the number of sources spatially distributed according to a Poisson distribution with mean value $\bar{N}$ in the patch, the probability that the total intensity at the origin is J is given by $P(J) = \sum_{N=0}^{\infty} P(N)P(J|N)$. By the inverse transform,

$$P(J|N) = \frac{1}{2\pi} \int_0^\infty \mathrm{e}^{-\mathrm{i}tJ} \mathcal{C}_1(t)^N \mathrm{d}t. \tag{A4}$$

Averaging over N,

$$P(J) = \sum_{N=0}^{\infty} \frac{\bar{N}^N \mathrm{e}^{-\bar{N}}}{N!} \frac{1}{2\pi} \int_0^\infty \mathrm{e}^{-\mathrm{i}tJ} \mathcal{C}_1(t)^N\ \mathrm{d}t \tag{A5}$$

$$= \frac{1}{2\pi} \int_0^\infty \mathrm{e}^{-\mathrm{i}tJ} \mathrm{e}^{\bar{N}[\mathcal{C}_1(t)-1]} \mathrm{d}t. \tag{A6}$$

Defining the characteristic function $\mathcal{C}(t) = \int_0^\infty \mathrm{e}^{\mathrm{i}tJ} P(J)\ \mathrm{d}J$, we find

$$\mathcal{C}(t) = \mathrm{e}^{\bar{N}[\mathcal{C}_1(t)-1]}. \tag{A7}$$

We may compute the mean background mean intensity from the standard formula $\langle J^n \rangle = (-\mathrm{i})^n\ \mathrm{d}^n \mathcal{C}(t)/\mathrm{d}t^n|_{t=0}$. The mean background intensity is then

$$\langle J \rangle = -\mathrm{i}\bar{N} \left. \frac{\mathrm{d}\mathcal{C}_1(t)}{\mathrm{d}t} \right|_{t=0} = \bar{N} \int_0^\infty jp(j)\ \mathrm{d}j = \bar{N}\bar{j}. \tag{A8}$$

We now construct a model for $p(j)$, assuming the luminosity and the position of a source are statistically independent. We may then express the probability distribution of $j(r, L)$ as $p(j)\ \mathrm{d}j = p(r)p(L)\ \mathrm{d}r\ \mathrm{d}L$. The probability distribution function of source luminosity is given by the luminosity function $\Phi(L)$ such that

$$p(L)\ \mathrm{d}L = \frac{\Phi(L)\ \mathrm{d}L}{\int_{L_{\min}}^\infty \Phi(L)\ \mathrm{d}L}, \tag{A9}$$

where $L_{\min}$ is the minimum luminosity of a source. Since the final result depends only on $\bar{L} = \int L\Phi(L)\ \mathrm{d}L$, which may be calibrated by the reionization fraction, we do not require the luminosity function of the high-redshift star-forming galaxies. The radial probability distribution is given as $p(r)\ \mathrm{d}r = 4\pi r^2 \mathrm{d}r/V$ for randomly distributed sources, where $V = 4\pi R^3/3$ is the proper volume of a spherical patch.

Thus, from equation (A8), we obtain

$$\langle J \rangle = \bar{n}_{\mathrm{s}} \frac{\bar{L}}{4\pi} \int_0^R \mathrm{e}^{-\tau(r)} \mathrm{d}r, \tag{A10}$$

where $\bar{n}_{\mathrm{s}} = \bar{N}/V$ is the proper number density of sources. Taking the patch radius to be the Ly*n* horizon, $R \to D_n^{\mathrm{hor}}$, gives

$$\langle J_n \rangle = \bar{n}_{\mathrm{s}} \frac{\bar{L}_{\nu_n}}{4\pi} \int_0^{D_n^{\mathrm{hor}}} \mathrm{e}^{-\tau_n(r)} \mathrm{d}r \tag{A11}$$

for the background Ly*n* mean intensity.

This paper has been typeset from a TEX/LATEX file prepared by the author.